

Angiography of the retina and the choroid with phase-resolved OCT using interval-optimized backstitched B-scans

Boy Braaf,^{1,*} Koenraad A. Vermeer,¹ Kari V. Vienola,¹ and Johannes F. de Boer^{1,2}

¹Rotterdam Ophthalmic Institute, Schiedamse Vest 160, 3011 BH Rotterdam, The Netherlands

²LaserLaB, Department of Physics and Astronomy, VU University, de Boelelaan 1081, 1081 HV Amsterdam, The Netherlands

*b.braaf@eyehospital.nl

Abstract: In conventional phase-resolved OCT blood flow is detected from phase changes between successive A-scans. Especially in high-speed OCT systems this results in a short evaluation time interval. This method is therefore often unable to visualize complete vascular networks since low flow velocities cause insufficient phase changes. This problem was solved by comparing B-scans instead of successive A-scans to enlarge the time interval. In this paper a detailed phase-noise analysis of our OCT system is presented in order to calculate the optimal time intervals for visualization of the vasculature of the human retina and choroid. High-resolution images of the vasculature of a healthy volunteer taken with various time intervals are presented to confirm this analysis. The imaging was performed with a backstitched B-scan in which pairs of small repeated B-scans are stitched together to independently control the time interval and the imaged lateral field size. A time interval of ≥ 2.5 ms was found effective to image the retinal vasculature down to the capillary level. The higher flow velocities of the choroid allowed a time interval of 0.64 ms to reveal its dense vasculature. Finally we analyzed depth-resolved histograms of volumetric phase-difference data to assess changes in amount of blood flow with depth. This analysis indicated different flow regimes in the retina and the choroid.

©2012 Optical Society of America

OCIS codes: (110.0110) Imaging systems; (170.3880) Medical and biological imaging; (110.4500) Optical coherence tomography; (170.4470) Ophthalmology; (280.2490) Flow diagnostics.

References and links

1. X. J. Wang, T. E. Milner, and J. S. Nelson, "Characterization of fluid flow velocity by optical Doppler tomography," *Opt. Lett.* **20**(11), 1337–1339 (1995).
2. J. A. Izatt, M. D. Kulkarni, S. Yazdanfar, J. K. Barton, and A. J. Welch, "In vivo bidirectional color Doppler flow imaging of picoliter blood volumes using optical coherence tomography," *Opt. Lett.* **22**(18), 1439–1441 (1997).
3. Y. Zhao, Z. Chen, C. Saxer, S. Xiang, J. F. de Boer, and J. S. Nelson, "Phase-resolved optical coherence tomography and optical Doppler tomography for imaging blood flow in human skin with fast scanning speed and high velocity sensitivity," *Opt. Lett.* **25**(2), 114–116 (2000).
4. S. Yazdanfar, A. M. Rollins, and J. A. Izatt, "Imaging and velocimetry of the human retinal circulation with color Doppler optical coherence tomography," *Opt. Lett.* **25**(19), 1448–1450 (2000).
5. S. Makita, Y. Hong, M. Yamanari, T. Yatagai, and Y. Yasuno, "Optical coherence angiography," *Opt. Express* **14**(17), 7821–7840 (2006).
6. R. K. Wang and S. Hurst, "Mapping of cerebro-vascular blood perfusion in mice with skin and skull intact by optical micro-angiography at 1.3 μm wavelength," *Opt. Express* **15**(18), 11402–11412 (2007).
7. B. J. Vakoc, R. M. Lanning, J. A. Tyrrell, T. P. Padera, L. A. Bartlett, T. Stylianopoulos, L. L. Munn, G. J. Tearney, D. Fukumura, R. K. Jain, and B. E. Bouma, "Three-dimensional microscopy of the tumor microenvironment in vivo using optical frequency domain imaging," *Nat. Med.* **15**(10), 1219–1223 (2009).
8. Z. Chen, T. E. Milner, D. Dave, and J. S. Nelson, "Optical Doppler tomographic imaging of fluid flow velocity in highly scattering media," *Opt. Lett.* **22**(1), 64–66 (1997).

9. B. White, M. Pierce, N. Nassif, B. Cense, B. Park, G. Tearney, B. Bouma, T. Chen, and J. de Boer, "In vivo dynamic human retinal blood flow imaging using ultra-high-speed spectral domain optical coherence tomography," *Opt. Express* **11**(25), 3490–3497 (2003).
10. R. Leitgeb, L. Schmetterer, W. Drexler, A. Fercher, R. Zawadzki, and T. Bajraszewski, "Real-time assessment of retinal blood flow with ultrafast acquisition by color Doppler Fourier domain optical coherence tomography," *Opt. Express* **11**(23), 3116–3121 (2003).
11. Y. Zhao, Z. Chen, C. Saxer, Q. Shen, S. Xiang, J. F. de Boer, and J. S. Nelson, "Doppler standard deviation imaging for clinical monitoring of in vivo human skin blood flow," *Opt. Lett.* **25**(18), 1358–1360 (2000).
12. L. Yu and Z. Chen, "Doppler variance imaging for three-dimensional retina and choroid angiography," *J. Biomed. Opt.* **15**(1), 016029 (2010).
13. D. Y. Kim, J. Fingler, J. S. Werner, D. M. Schwartz, S. E. Fraser, and R. J. Zawadzki, "In vivo volumetric imaging of human retinal circulation with phase-variance optical coherence tomography," *Biomed. Opt. Express* **2**(6), 1504–1513 (2011).
14. J. Fingler, D. Schwartz, C. Yang, and S. E. Fraser, "Mobility and transverse flow visualization using phase variance contrast with spectral domain optical coherence tomography," *Opt. Express* **15**(20), 12636–12653 (2007).
15. L. An, H. M. Subhush, D. J. Wilson, and R. K. Wang, "High-resolution wide-field imaging of retinal and choroidal blood perfusion with optical microangiography," *J. Biomed. Opt.* **15**(2), 026011 (2010).
16. M. Szkulmowski, A. Szkulmowska, T. Bajraszewski, A. Kowalczyk, and M. Wojtkowski, "Flow velocity estimation using joint spectral and time domain optical coherence tomography," *Opt. Express* **16**(9), 6008–6025 (2008).
17. A. H. Bachmann, M. L. Villiger, C. Blatter, T. Lasser, and R. A. Leitgeb, "Resonant Doppler flow imaging and optical vivisection of retinal blood vessels," *Opt. Express* **15**(2), 408–422 (2007).
18. V. X. D. Yang, M. L. Gordon, A. Mok, Y. H. Zhao, Z. P. Chen, R. S. C. Cobbold, B. C. Wilson, and I. A. Vitkin, "Improved phase-resolved optical Doppler tomography using the Kasai velocity estimator and histogram segmentation," *Opt. Commun.* **208**(4-6), 209–214 (2002).
19. B. Park, M. C. Pierce, B. Cense, S. H. Yun, M. Mujat, G. Tearney, B. Bouma, and J. de Boer, "Real-time fiber-based multi-functional spectral-domain optical coherence tomography at 1.3 microm," *Opt. Express* **13**(11), 3931–3944 (2005).
20. Y. Wang, B. A. Bower, J. A. Izatt, O. Tan, and D. Huang, "Retinal blood flow measurement by circumpapillary Fourier domain Doppler optical coherence tomography," *J. Biomed. Opt.* **13**(6), 064003 (2008).
21. A. S. Singh, C. Kolbitsch, T. Schmoll, and R. A. Leitgeb, "Stable absolute flow estimation with Doppler OCT based on virtual circumpapillary scans," *Biomed. Opt. Express* **1**(4), 1047–1058 (2010).
22. I. Grulkowski, I. Gorczynska, M. Szkulmowski, D. Szlag, A. Szkulmowska, R. A. Leitgeb, A. Kowalczyk, and M. Wojtkowski, "Scanning protocols dedicated to smart velocity ranging in spectral OCT," *Opt. Express* **17**(26), 23736–23754 (2009).
23. S. Makita, T. Fabritius, and Y. Yasuno, "Quantitative retinal-blood flow measurement with three-dimensional vessel geometry determination using ultrahigh-resolution Doppler optical coherence angiography," *Opt. Lett.* **33**(8), 836–838 (2008).
24. M. R. Hee, *Optical Coherence Tomography of the Eye* (Massachusetts Institute of Technology, 1997).
25. B. Braaf, K. A. Vermeer, V. A. Sicam, E. van Zeeburg, J. C. van Meurs, and J. F. de Boer, "Phase-stabilized optical frequency domain imaging at 1- μ m for the measurement of blood flow in the human choroid," *Opt. Express* **19**(21), 20886–20903 (2011).
26. S. Makita, J. Franck, M. Yamanari, M. Miura, and Y. Yasuno, "Comprehensive in vivo micro-vascular imaging of the human eye by dual-beam-scan Doppler optical coherence angiography," *Opt. Express* **19**(2), 1271–1283 (2011).
27. S. Zotter, M. Pircher, T. Torzicky, M. Bonesi, E. Götzinger, R. A. Leitgeb, and C. K. Hitzenberger, "Visualization of microvasculature by dual-beam phase-resolved Doppler optical coherence tomography," *Opt. Express* **19**(2), 1217–1227 (2011).
28. R. D. Ferguson, D. X. Hammer, L. A. Paunescu, S. Beaton, and J. S. Schuman, "Tracking optical coherence tomography," *Opt. Lett.* **29**(18), 2139–2141 (2004).
29. S. Ricco, M. Chen, H. Ishikawa, G. Wollstein, and J. Schuman, "Correcting motion artifacts in retinal spectral domain optical coherence tomography via image registration," *Med. Image Comput. Comput. Assist. Interv.* **12**(Pt 1), 100–107 (2009).
30. R. de Kinkelder, J. Kalkman, D. J. Faber, O. Schraa, P. H. Kok, F. D. Verbraak, and T. G. van Leeuwen, "Heartbeat-induced axial motion artifacts in optical coherence tomography measurements of the retina," *Invest. Ophthalmol. Vis. Sci.* **52**(6), 3908–3913 (2011).
31. B. Vakoc, S. Yun, J. de Boer, G. Tearney, and B. Bouma, "Phase-resolved optical frequency domain imaging," *Opt. Express* **13**(14), 5483–5493 (2005).
32. G. Bennett and R. B. Rabbetts, "Distribution and ocular dioptries of ametropia," in *Bennett and Rabbetts' Clinical Visual Optics*, R. B. Rabbetts, ed. (Elsevier Science, 1998), pp. 406–420.
33. A. Agarwal, *Grass' Atlas of Macular Diseases* (Elsevier Saunders, 2012).
34. C. E. Riva and L. Schmetterer, "Microcirculation of the ocular fundus," in *Comprehensive Physiology*, (Wiley-Blackwell, 2011), pp. 735–765.
35. Z. Burgansky-Eliash, D. A. Nelson, O. P. Bar-Tal, A. Lowenstein, A. Grinvald, and A. Barak, "Reduced retinal blood flow velocity in diabetic retinopathy," *Retina* **30**(5), 765–773 (2010).
36. T. J. Fallon, P. Chowienczyk, and E. M. Kohner, "Measurement of retinal blood flow in diabetes by the blue-light entoptic phenomenon," *Br. J. Ophthalmol.* **70**(1), 43–46 (1986).

37. P. Hossain, J. Liversidge, M. J. Cree, A. Manivannan, P. Vieira, P. F. Sharp, G. C. Brown, and J. V. Forrester, "In vivo cell tracking by scanning laser ophthalmoscopy: quantification of leukocyte kinetics," *Invest. Ophthalmol. Vis. Sci.* **39**(10), 1879–1887 (1998).
38. T. Okanouchi, F. Shiraga, I. Takasu, Y. Tsuchida, and H. Ohtsuki, "Evaluation of the dynamics of choroidal circulation in experimental acute hypertension using indocyanine green-stained leukocytes," *Jpn. J. Ophthalmol.* **47**(6), 572–577 (2003).
39. L. Zhu, Y. Zheng, C. H. von Kerczek, L. D. Topoleski, and R. W. Flower, "Feasibility of extracting velocity distribution in choriocapillaris in human eyes from ICG dye angiograms," *J. Biomech. Eng.* **128**(2), 203–209 (2006).
40. R. W. Flower, A. W. Fryczkowski, and D. S. McLeod, "Variability in choriocapillaris blood flow distribution," *Invest. Ophthalmol. Vis. Sci.* **36**(7), 1247–1258 (1995).
41. I. Takasu, F. Shiraga, T. Okanouchi, Y. Tsuchida, and H. Ohtsuki, "Evaluation of leukocyte dynamics in choroidal circulation with indocyanine green-stained leukocytes," *Invest. Ophthalmol. Vis. Sci.* **41**(10), 2844–2848 (2000).
42. V. F. Duma, K. S. Lee, P. Meemon, and J. P. Rolland, "Experimental investigations of the scanning functions of galvanometer-based scanners with applications in OCT," *Appl. Opt.* **50**(29), 5735–5749 (2011).
43. S. Jiao, R. Knighton, X. Huang, G. Gregori, and C. Puliafito, "Simultaneous acquisition of sectional and fundus ophthalmic images with spectral-domain optical coherence tomography," *Opt. Express* **13**(2), 444–452 (2005).
44. Q. Yang, D. W. Arathorn, P. Tiruveedhula, C. R. Vogel, and A. Roorda, "Design of an integrated hardware interface for AOSLO image capture and cone-targeted stimulus delivery," *Opt. Express* **18**(17), 17841–17858 (2010).
45. A. W. Fryczkowski and M. D. Sherman, "Scanning electron microscopy of human ocular vascular casts: the submacular choriocapillaris," *Acta Anat. (Basel)* **132**(4), 265–269 (1988).
46. M. Szkulmowski, I. Gorczynska, D. Szlag, M. Sylwestrzak, A. Kowalczyk, and M. Wojtkowski, "Efficient reduction of speckle noise in optical coherence tomography," *Opt. Express* **20**(2), 1337–1359 (2012).
47. F. Jaillon, S. Makita, and Y. Yasuno, "Variable velocity range imaging of the choroid with dual-beam optical coherence angiography," *Opt. Express* **20**(1), 385–396 (2012).
48. M. K. Leung, A. Mariampillai, B. A. Standish, K. K. Lee, N. R. Munce, I. A. Vitkin, and V. X. Yang, "High-power wavelength-swept laser in Littman telescope-less polygon filter and dual-amplifier configuration for multichannel optical coherence tomography," *Opt. Lett.* **34**(18), 2814–2816 (2009).
49. L. A. Yannuzzi, K. T. Rohrer, L. J. Tindel, R. S. Sobel, M. A. Costanza, W. Shields, and E. Zang, "Fluorescein angiography complication survey," *Ophthalmology* **93**(5), 611–617 (1986).
50. M. Hope-Ross, L. A. Yannuzzi, E. S. Gragoudas, D. R. Guyer, J. S. Slakter, J. A. Sorenson, S. Krupsky, D. A. Orlock, and C. A. Puliafito, "Adverse reactions due to indocyanine green," *Ophthalmology* **101**(3), 529–533 (1994).
51. J. E. Grunwald, T. I. Metelitsina, J. C. Dupont, G. S. Ying, and M. G. Maguire, "Reduced foveolar choroidal blood flow in eyes with increasing AMD severity," *Invest. Ophthalmol. Vis. Sci.* **46**(3), 1033–1038 (2005).
52. E. Koch, J. Walther, and M. Cuevas, "Limits of Fourier domain Doppler-OCT at high velocities," *Sens. Actuators A-Phys.* **156**(1), 8–13 (2009).
53. H. Ren, K. M. Brecke, Z. Ding, Y. Zhao, J. S. Nelson, and Z. Chen, "Imaging and quantifying transverse flow velocity with the Doppler bandwidth in a phase-resolved functional optical coherence tomography," *Opt. Lett.* **27**(6), 409–411 (2002).

1. Introduction and theory

Angiographic imaging has become a popular functional extension of optical coherence tomography (OCT) since its introduction for the imaging of blood flow in the skin [1–3]. The non-invasive character and high axial (2–15 μm) and lateral (5–30 μm) resolution of OCT are well suited to visualize *in vivo* vascular networks of e.g. the eye [4,5], the skin [3], the brain [6], and in microscopy applications on *in vitro* tissues [7]. The angiographic imaging extension of OCT is commonly known as Doppler OCT or phase-resolved OCT and discriminates (blood) flow from static tissues by phase changes in the OCT signal caused by moving light-scattering particles [1,8]. Various implementations of this technique have been published including phase-resolved Doppler OCT [3,9,10], phase-variance OCT [11–14], optical micro-angiography [6,15], joint spectral-time domain OCT [16], and resonant Doppler flow imaging [17]. Among these implementations phase-resolved Doppler OCT is the most popular since it is easily implemented on standard Fourier-Domain OCT hardware and software [9,10] and can provide qualitative (vasculature imaging) as well as quantitative (flow velocity determination) information on perfusion.

In phase-resolved Doppler OCT blood flow is detected from the phase difference $\Delta\phi$ between two A-scans [3]:

$$\Delta\phi = \frac{4\pi n \tau v_{flow}}{\lambda_0} \cos(\alpha), \quad (1)$$

in which n is the refractive index of the tissue, τ is the time interval between the two A-scans, v_{flow} is the blood flow velocity, λ_0 is the center wavelength of the OCT light source, and α is the angle between the flow velocity direction and the OCT-beam which is also known as the Doppler angle. Equation (1) shows the limitations of phase-resolved Doppler OCT. In case of slow blood flows (low v_{flow}), a small time interval (small τ), or a steep Doppler angle (small $\cos(\alpha)$) the observed phase-difference becomes very low and potentially indistinguishable from noise. The noise on the phase-difference, the phase-noise $\sigma_{\Delta\phi}$, defines therefore the minimum flow velocity that can be observed: $v_{min} = (\sigma_{\Delta\phi} \lambda_0) / (4\pi n \tau \cos(\alpha))$ [10,18]. The phase-noise follows a Gaussian probability distribution for which the standard deviation depends on the signal-to-noise ratio (SNR) and on noise caused by a imperfect spot-overlap between the compared A-scans [19]:

$$\sigma_{\Delta\phi} = \sqrt{\left(\frac{1}{SNR_s}\right) + \left(\frac{4\pi}{3}\right) \left(1 - \exp\left(-2\left(\frac{\Delta x}{d}\right)^2\right)\right)}. \quad (2)$$

In Eq. (2) SNR_s is the ratio of the OCT sample signal strength and the mean noise floor, d the spot diameter of the OCT-bundle on the sample, and Δx is the spot displacement between the two A-scans. A high phase-noise due to a low SNR_s or a high $\Delta x/d$ ratio results in a high v_{min} and makes the observation of blood flow therefore more difficult.

In ophthalmic applications the Doppler angle ranges from 70° to 90° for vessels around the optic nerve head [20,21] while at the macula and most other locations it is nearly 90° [22,23]. These steep angles are a result of the parallel orientation of the vasculature with respect to the retinal surface and the nearly perpendicular incidence of the OCT-light [24]. In conventional phase-resolved Doppler OCT blood flow is detected from successive A-scans which results in small values for the time interval τ for high-speed OCT systems. The unfortunate combination with steep Doppler angles limits the visualization of ocular vasculature to larger arteries and veins [25].

In order to improve the flow sensitivity of ophthalmic phase-resolved Doppler OCT alternative methods have been investigated to increase the time interval τ while reducing the spot displacement Δx . Grulkowski *et al.* have proposed to use repetitive backstitched (segmented) triangle and sawtooth waveforms to drive the fast axis scanner [22]. This method enabled repeated B-scan measurements of the same sample location with a user-defined time interval, but reduced the imaging acquisition speed by at least 50%. Makita *et al.* and Zotter *et al.* proposed another method called dual-beam phase-resolved Doppler OCT in which two OCT-beams are used that are separated along the fast axis direction [26,27]. This allows the simultaneous acquisition of two B-scans of the same sample location separated in time without compromising on the acquisition speed, but with increased hardware complexity and a 3 dB sensitivity loss as a consequence. In both techniques the inter-B-scan comparison enabled imaging of the micro-vasculature network of the retina. However, a detailed analysis on the phase-noise during *in vivo* measurements and consequently how to select the optimal time interval for phase-resolved imaging of a specific vasculature type has never been described.

In this paper we therefore measured the phase-noise during OCT-measurements in order to calculate the minimum observable flow velocity for different time intervals. This was done on a phase-stabilized optical frequency domain imaging (OFDI) system for which we previously demonstrated a very low phase-noise performance of the interferometer [25]. This instrument is therefore ideal to measure the phase-noise contributions of galvanometer scanning action and sample movement which are expected to increase for longer time intervals. Consequently, the required inter-B-scan time interval for imaging of a specific vasculature type was

estimated by comparison with known flow velocities from literature. These results were used for inter-B-scan phase-resolved imaging of the (micro-)vasculature of the retina and choroid with backstitched B-scans similar as described by Grulkowski *et al.* [22] Using this method we show, to our knowledge, the first wide-field images of the retinal and choroidal (micro-)vasculature made with phase-resolved OFDI. Further, a new method to assess the amount of blood flow is presented based on histogram analysis of volumetric phase-difference data. This method indicated different flow regimes with depth in the retina and choroid.

2. Experimental system description

2.1 Phase-resolved optical frequency domain imaging setup

The OFDI setup used in this study was developed and described earlier by our group [25]. Only the sample arm optics were modified to improve the OCT imaging as specified below.

In summary the setup uses a 1- μm swept-source with a fixed repetition rate of 100 kHz (Axsun technologies) and a fiber-based interferometer with an axial resolution of 4.8 μm (6.5 μm in air). The low relative intensity noise of the swept-source, careful adjustment of the reference arm power, and the use of balanced detection enabled a system operation < 1 dB from the shot-noise. In order to calibrate and phase-stabilize the OCT measurements a parallel Mach-Zehnder interferometer was embedded in the setup to map A-scan spectra to the same wavenumbers (k-space). This enabled the suppression of fixed-pattern noise and phase-artifacts to negligible levels [25].

In the sample arm of the interferometer a standard ophthalmic OCT scanning system with galvanometer scanners (Cambridge technology 6220, 5 mm mirrors) and a demagnifying telescope was used to image the retina and choroid. Light losses were minimized by replacing its 40D Volk lens for a stacked pair of common 50 mm NIR AR-coated achromatic lenses. The beam diameter ($1/e^2$) on the cornea was 0.88 mm for this study and provided a theoretical diffraction-limited retinal spot-size of 25.2 μm . The optical power on the cornea was 1.8 mW. The system sensitivity was measured to be 101.7 dB which is a 2.6 dB improvement over our previous configuration [25]. This is mainly due to the lower light loss on the ophthalmic lens.

2.2 Sample motion minimization and correction

During *in vivo* ophthalmic OCT measurements the retinal tissue is subject to movement due to a variety of reasons including involuntary eye movements [28,29] and the cardiac cycle [30]. Lateral movement causes decorrelation of the A-scans which disrupts phase-resolved OCT imaging. In this study lateral eye motion was therefore minimized by providing a fixation target to the subject. Axial movement displaces the information of an A-scan along depth and can be corrected relatively easy in post-processing using e.g. subtraction of the median or weighted mean phase-difference [9,31], or histogram-based normalization [5,18]. In these methods pixels are usually treated as separate units and the information exchange in between pixels due to motion is ignored. This potentially leads to an under-correction of the axial motion when the displacement between the compared A-scans is substantial.

In this study a two-step correction algorithm is therefore implemented that first reduces large axial displacements to sub-pixel accuracy and afterwards applies an existing method. Large axial displacements were estimated with cross-correlation from the axial (sub-)pixel shift in between the intensity images of the compared B-scans. The found shift Δp is corrected by multiplication of the OCT signals $S_{oct}(k)$ of the second B-scan with a complex exponential function: $\tilde{S}_{oct}(k) = S_{oct}(k) \cdot \exp(-i 2\pi k \Delta p)$. Afterwards any remaining axial displacement was corrected using histogram-based normalization similar as described by Makita *et al* [5].

2.3 Ethical considerations

The use of our experimental setup for *in vivo* measurements in humans was approved by the local Institutional Review Board and adhered to the tenets of the Declaration of Helsinki. Informed consent was obtained from each subject.

3. Phase-noise analysis and time interval calculations

Optimal system performance for phase-resolved OCT is achieved when the phase-noise is dominated by its SNR-component [25,31]. This condition requires the phase-noise contribution due to spot displacement to be low. We therefore analyzed the phase-noise contributions of the physically moving parts: the galvanometer scanners (section 3.1) and the sample (section 3.2). Based on these results we evaluated if SNR-limited performance can be achieved (section 3.3) and calculated the observable flow velocities as a function of time interval (section 3.4). Optimal time intervals to image retinal and choroidal vasculature are selected by comparison with flow velocity values found in literature (section 3.4). In the analysis we assumed that axial displacements were corrected to negligible levels. Similarly we left the phase-noise contribution of the OFDI interferometer out of the analysis since we showed earlier that it contributes a negligible amount of less than 5 mrad [25].

3.1 Phase-noise due the galvanometer scanners

The phase-noise contribution of the galvanometer scanners was measured in a model eye to prevent interference by sample motion. The model eye consisted of a 60D lens and a plastic slab that acted as an artificial retina. The power of the model eye is equal to the average human eye [32] and the spot-size and beam-displacements on the plastic slab were therefore similar as found *in vivo* on the human retina.

The static galvanometer noise was measured by imaging the artificial retina at the exact same location without scanning the OCT-beam. A number of 10,000 A-scans was acquired and phase-difference values were calculated by subtracting a time-shifted version of the data from the original data. The amount of time-shifting was varied to obtain phase-differences at different time intervals up to 5 ms. The phase-noise was determined by the standard deviation of the phase-difference values. Pixels from outside the sample were excluded using a threshold on the SNR. The contribution of the SNR_s was subtracted to isolate the phase-noise due to the galvanometer scanners. The measurement was performed 10 times and the mean \pm the standard deviation of the phase-noise is reported. This experiment was performed both when the galvanometer electronics were switched *off* and *on* to demonstrate a phase-noise increase in the latter case. An example is shown in Fig. 1(A) in which stable structures are seen in the intensity image (top) and the phase-difference image (bottom).

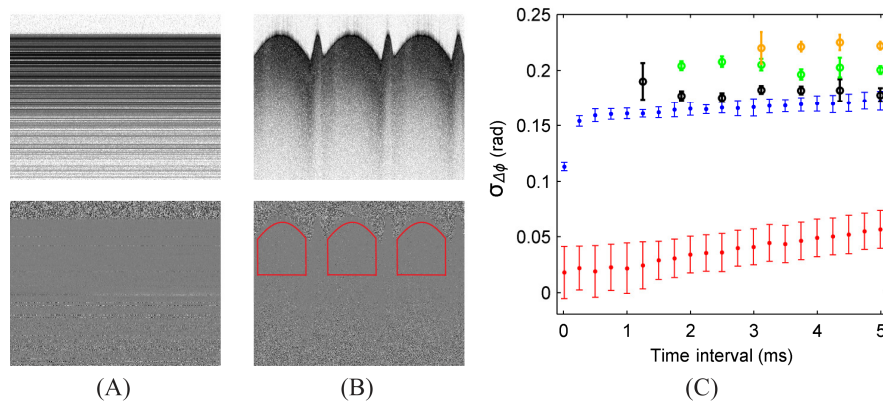


Fig. 1. Phase-noise measurement in a model eye. (A) The static galvanometer scanner noise was measured without scanning the OCT beam. (B) The dynamic galvanometer scanner noise was determined by measuring the phase-noise from inter-B-scan phase-difference values from successive B-scans. In both (A) and (B) examples of the experiment are shown with the intensity image at the top and the phase-difference image at the bottom. (C) The phase-noise as a function of the time interval and lateral scan width. The phase-noise is plotted when the galvanometer scanners are switched off (red), switched on but kept still (blue), and scanned over three lateral scan widths: 1.05 mm (black), 4.21 mm (green), and 8.56 mm (orange). The galvanometer scanners cause a significant amount of phase-noise which is attributed to electrical noise and scanning errors.

In Fig. 1(C) in red the phase-noise is given when the galvanometer scanner electronics are switched *off*. The phase-noise slowly increases over time due to small environmental vibrations up to 0.06 ± 0.02 rad for a time interval of 5.0 ms (500 A-scans). In blue the phase-noise is given when the galvanometer scanners electronics are switched *on* and kept at a stationary location. In this case the phase-noise rapidly increases within the first 0.25 ms (25 A-scans) which is attributed to electrical noise within the galvanometer system. The phase-noise is however stabilized by the galvanometer correction feedback for longer time intervals to a level below 0.17 rad. The equivalent spot displacement corresponding to this noise is 1.5 μm .

The dynamic galvanometer noise was measured by acquiring multiple B-scans at the same location of the artificial retina using a sawtooth as the waveform for the fast axis scanner. The phase-noise was calculated by the standard deviation of the phase-differences from consecutive B-scans. In order to assess different time intervals (up to 5 ms) the amount of A-scans per B-scan was varied. The A-scans during the mirror fly-back were excluded from the analysis, as well as pixels from outside the sample. Additionally the lateral scan width of the B-scans was varied to measure the phase-noise response for increased scan velocities. The phase-noise contribution of the SNR_s was removed. These measurements were performed four times and the mean \pm the standard deviation of the phase-noise is reported. An example is shown in Fig. 1(B) in which the intensity image (top) and the inter-B-scan phase-difference image (bottom) is shown for three consecutive B-scans.

The inter-B-scan phase-noise was measured for three lateral scan widths: 1.05 mm, 4.21 mm, and 8.56 mm which are plotted in Fig. 1(C) in respectively black, green and orange. The dynamic galvanometer phase-noise is higher than the static galvanometer phase-noise which is attributed to errors in revisiting the same location. This error increases for faster scan velocities. The results further suggest that for scan widths below 1.05 mm the phase-noise will be dominated by the static galvanometer noise.

Overall it can be concluded that the galvanometer scanners cause a significant amount of phase-noise that cannot be neglected, especially for longer time intervals.

3.2 Phase-noise due to sample motion

The phase-noise contribution of sample motion was measured in a healthy volunteer with the galvanometer scanners switched *off*. This experiment was performed and analyzed equivalent to the static experiment described in section 3.1. An example is displayed in Fig. 2(A) which shows the same retinal location for a period of 0.1 s (10,000 A-scans). During the measurement the subject was asked to look at the fixation light as is done during regular OCT-imaging. Artifacts due to blood flow were avoided by selection of the retinal pigment epithelium (RPE) tissue layer, which contains a minimal amount of vasculature. This is shown in red in the bottom figure of Fig. 2(A). The measurement was performed 10 times and the mean \pm the standard deviation of the phase-noise is reported.

The results are given in Fig. 2(B) in black and the phase-noise of the switched-on galvanometer scanning system is added in blue for comparison. The phase-noise due to sample motion increases rapidly over time to 0.59 ± 0.23 rad for a time interval of 5.0 ms (500 A-scans). In comparison with the static galvanometer scanners the phase-noise due to sample motion is dominant for time intervals above 0.25 ms (25 A-scans). This indicates that the system phase-noise is dominated by sample motion.

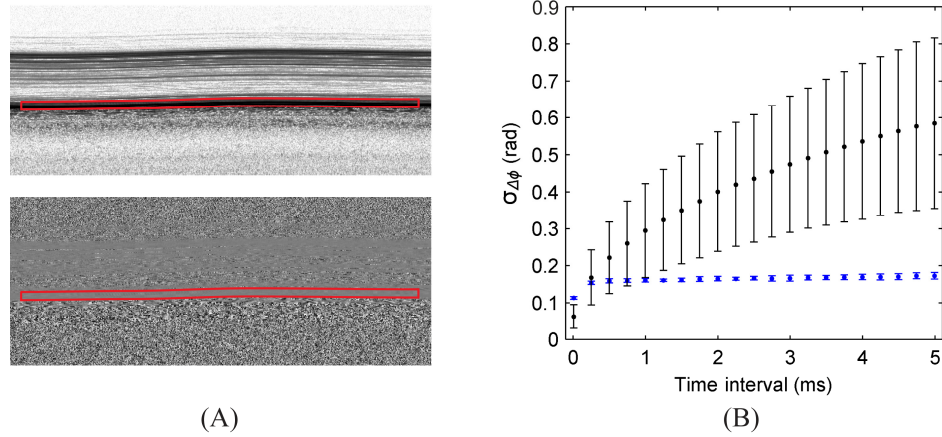


Fig. 2. *In vivo* phase-noise measurement due to sample motion. (A) The scanners were off and A-scans were acquired for a period of 0.1s (10,000 A-scans). The top figure shows the intensity image, the bottom figure shows the phase-difference image for a time interval of 1.0 ms (100 A-scans). The phase-noise was analyzed from the RPE layer (red box) to avoid interference with blood flow. (B) The phase-noise due to sample motion (black) and the static galvanometer scanner phase-noise (blue) from Fig. 1 as a function of the time interval. The phase-noise due to sample motion becomes dominant for time intervals above 0.25 ms (25 A-scans).

3.3 SNR-limited performance analysis

In the optimal situation the phase-noise is only limited by the SNR_s , hence $\sigma_{\Delta\phi} = \sqrt{1/\text{SNR}_s}$. In order to verify for which SNR levels this situation occurs the OFDI system phase-noise is estimated conservatively by the quadratic addition of the phase-noise from the static galvanometer scanning system and the sample motion: $\sigma_{\Delta\phi} = \sqrt{(\sigma_{\text{galvo}}^2 + \sigma_{\text{motion}}^2)}$. The equivalent SNR_s to this system phase-noise is plotted in Fig. 3 in which values below the red line indicate domination of the phase-noise by the SNR_s .

For all time intervals the equivalent SNR_s -levels fall below 20 dB which is lower than expected for normal imaging conditions. This indicates that SNR-limited performance is not achieved and the phase-noise is dominated by the galvanometer scanners and sample motion. Further it indicates that the phase-noise due to the SNR can be neglected in the majority of the measurements as is done in the remainder of the paper. However, note that deep in the choroid the SNR_s could be significantly lower and SNR-dominated phase-noise might occur.

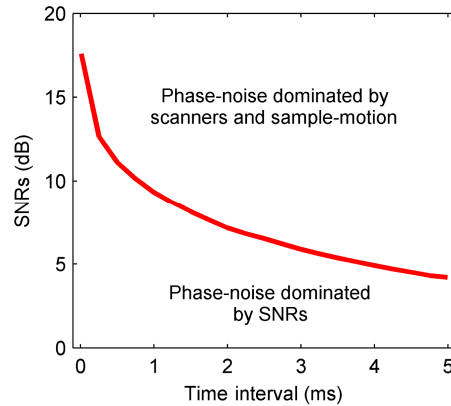


Fig. 3. The SNR_s -levels as a function of the time interval that give an equivalent amount of phase-noise as the combined phase-noise of the galvanometer scanners and sample motion. The phase-noise is dominated by the SNR_s if the SNR of a measurement falls below the red line.

3.4 Observable flow velocities and time interval calculations

Considering only *absolute* flow velocities, the lowest observable flow velocity can be calculated from the total phase-noise using Eq. (1). Similarly, the highest flow velocity that can be observed unambiguously is given by the maximum phase-difference of π . Faster flow velocities undergo phase wrapping and appear aliased at lower velocities, which can still be observed as long as their wrapped phase-difference exceeds the phase-noise ($|\Delta\phi| \geq \sigma_{\Delta\phi}$). In contrary to quantitative analysis phase wrapping is of limited concern for qualitative imaging of blood flow. Taking phase-wrapping into account the observable flow velocities were calculated from the system phase-noise (section 3.3) as a function of time interval and Doppler angle. This was done for near-perpendicular angles of 85° and 89° that are expected to reside within the macular area which is shown in Fig. 4(A) and 4(B) respectively. The blue areas indicate observable flow velocities and in between white strips mark unobservable flow velocities that are wrapped into the phase-noise. Note that the flow velocity on the y-axis is the actual velocity within a blood vessel.

Figure 4 shows that for a smaller Doppler angle phase-wrapping occurs more frequent, although the strips dominated by the phase-noise are smaller. Further it is noticeable that flow velocities lower than 1 mm/s can already be imaged with time intervals above 1 ms at the steepest Doppler angle of 89° .

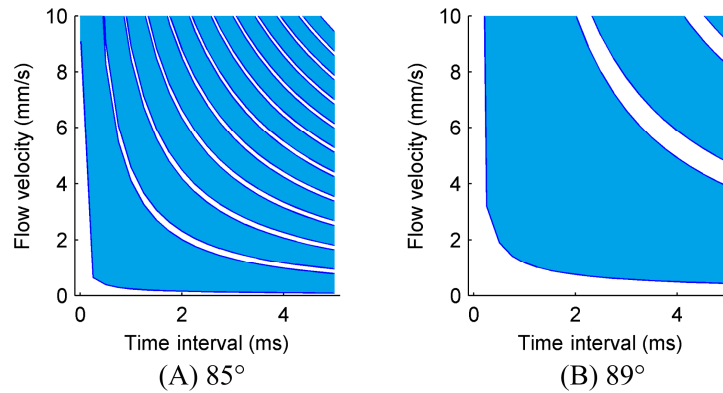


Fig. 4. Observable flow velocities as a function of the time interval for Doppler angles of 85° (A) and 89° (B). The blue areas indicate observable flow velocities for which the wrapped phase-difference signals exceed the phase-noise. The white areas indicate unobservable flow velocities that are buried in the phase-noise.

In order to visualize a specific (micro-)vascular type the time interval has to be optimized to match the measurable flow velocity range with the *in vivo* flow velocities. In healthy individuals both the retinal and choroidal circulation can be subdivided into three distinct levels according to vessel size and therefore flow velocity [33]. In the retina several central arteries and veins branch out into arterioles and venules (small arteries and veins) which are interconnected via capillary beds. Similar, in the choroid the posterior ciliary arteries and veins branch out in arterioles and venules which interconnect in the extremely dense capillary bed of the choriocapillaris. In Table 1 the known velocity range of each vasculature type is summarized. Using these velocity ranges the corresponding time interval ranges can be derived from Fig. 4 for Doppler angles of 85° and 89° . It can be seen from Table 1 that especially for the imaging of capillary flow long time intervals (>1 ms) are necessary. Further even the fast flow in the central retinal arteries and veins and the posterior ciliary arteries and veins are expected to be (partially) unobservable at steep Doppler angles of 89° with conventional phase-resolved OCT. The predicted time intervals are compared to experimental data in section 5.

Table 1. Flow velocity ranges for the retinal and the choroidal vasculature and the corresponding time intervals that are required for imaging phase-resolved OCT. The time intervals are given for Doppler angles of 85° and 89° that are expected to reside within the macular region. *Partially obtained from animal studies.

Vasculature	Velocity range (mm/s)	Time interval range (ms)	
		85°	89°
Retinal central arteries & veins	17 – 190 [34]	< 0.01	0.17 – < 0.01
Retinal arterioles & venules	1.8 – 7.2 [34,35]	0.22 – 0.07	0.56 – 0.23
Retinal capillaries	0.2 – 3.3 [34,36]	1.28 – 0.18	9.75 – 0.25
Posterior ciliary arteries & veins	17 – 140 [34]	< 0.01	0.17 – < 0.01
Choroidal arterioles & venules	5.5 – 12 [37,38]*	0.11 – < 0.01	0.24 – 0.20
Choriocapillaris	0.3 – 3.6 [39–41]*	0.72 – 0.17	7.15 – 0.25

4. Backstitched B-scans for imaging at long time intervals

As calculated in Table 1, the time in between A-scans (0.01 ms) is too small to visualize all vascular types and should be extended to several milliseconds to observe capillary blood flows. Inter-B-scan comparison is therefore used in this study to achieve these increased time intervals by acquiring two B-scans at each location. In order to limit the spot displacement due to eye motion, the time interval in between two B-scans (the number of A-scans of a single B-scan) is best taken as small as possible. This results in B-scans that cover a limited lateral scan width if a high lateral sampling density is used to observe small vasculature. Subsequently, a larger lateral scan width can be achieved by stitching multiple sets of repeated B-scans together along the fast-axis direction to create a *backstitched B-scan*. This method gives independent control over the time interval and the lateral scan width and is similar to the segmented B-scan protocols used by Grulkowski *et al.* [22].

In Fig. 5(A) an example of our implementation of the waveform of the backstitched B-scan is plotted as a blue curve with its corresponding OCT intensity image on the background. The waveform has a quasi-sawtooth shape in which one tooth corresponds to one complete B-scan that includes forward lateral scanning over the retina (increasing slope) and a rapid flyback to its initial position (decreasing slope). In Fig. 5(A) a single B-scan has been marked with a solid orange box. Every complete B-scan is followed by a second B-scan without flyback (only increasing slope) to rescan the same locations on the retina for which an example is marked by the dashed orange box. The combination of a complete B-scan and a B-scan without flyback is called a set of repeated B-scans and is used in series at adjacent lateral locations. A series of four sets of repeated B-scans is shown in Fig. 5(A) after which a large flyback completes the backstitched B-scan waveform (right from the yellow dashed line). In post-processing two normal B-scans without flyback (Fig. 5(B) and 5(C)) are reconstructed from the backstitched B-scan to calculate the inter-B-scan phase-difference image (shown in next section).

In practice the actual galvanometer scanner motion deviates from the quasi-sawtooth waveform during the rapid flyback parts due to the inertia of the scanner [42]. This effect obstructs a complete flyback to the initial location of a B-scan and consequently a small part at the beginning of each set of repeated B-scans is unusable for inter-B-scan phase-resolved measurements. This results in a small *gap* in the phase-resolved data between neighboring sets of repeated B-scans. As a solution a small lateral overlap in between adjacent sets of repeated B-scans was included into the backstitched B-scan waveform. This is shown in the magnified inset (red solid box) in Fig. 5(A) in which the overlap is marked in green. The overlap assures that the data at the end of the previous set of repeated B-scans fills the *gap* of the next set. The *gaps* and any surplus in overlap were omitted from the reconstructed B-scans (Fig. 5(B) and 5(C)).

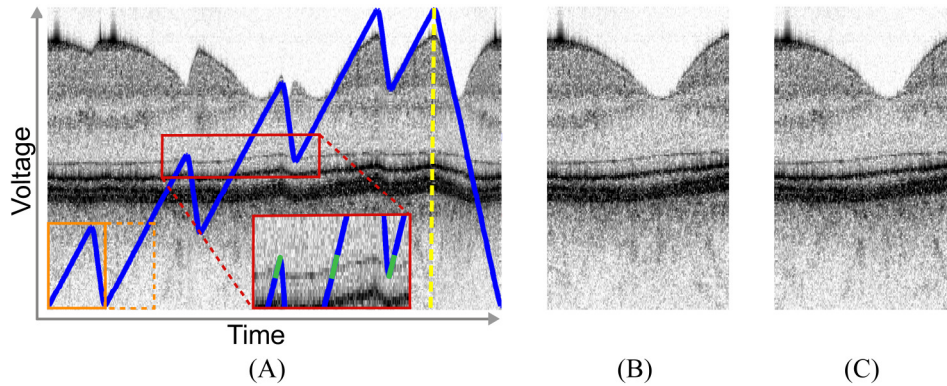


Fig. 5. (A) An example of the backstitched B-scan (in blue) that is used for inter-B-scan phase-resolved OFDI imaging with a time interval of 2.5 ms (250 A-scans). The corresponding intensity image is plotted in the background. An example of a single B-scan is marked by the solid orange box. The subsequent B-scan without flyback is marked by the dashed orange box. In order to prevent gaps in between successive sets of repeated B-scans a small overlap is used as shown in green in the inset. The backstitched B-scan returns to its initial location with a long flyback as shown right from the yellow line. (B&C) The B-scans over the full lateral scan width as reconstructed from the backstitched B-scan corresponding respectively to the first (B) and second (C) B-scan of each set.

In this study various time intervals were used to confirm their effect on the visualized vasculature as calculated in section 3.4. The inter-B-scan time intervals used were 0.64 ms (64 A-scans), 1.25 ms (125 A-scans), 2.50 ms (250 A-scans), 3.75 ms (375 A-scans), and 5.00 ms (500 A-scans). For comparative purposes also the conventional phase-resolved Doppler method was included for which the time interval is defined by the A-scan rate of the swept-source: 0.01 ms (1 A-scan). The properties of the backstitched waveforms used for these time intervals are summarized in Table 2. Each backstitched B-scan covered a lateral width of 2.1 mm and the scan-width of an individual small B-scan never exceeded 1.05 mm. A fraction of 20% of the backstitched B-scans was taken as flyback to ensure similar phase-noise conditions as in section 3.

A disadvantage of backstitched B-scans is the increased amount of lateral overlap and flyback compared to conventional B-scans. This results in a decrease of the number of A-scans that are included in a reconstructed B-scan and therefore in a lower effective acquisition speed. We express this effect in the *Doppler B-scan duty cycle* which is defined as the fraction of the number of A-scans of a single reconstructed B-scan and the number of A-scans of a complete backstitched B-scan. The theoretical limit for the duty cycle of backstitched B-scans would be 50% in the absence of flyback and overlap. As can be seen in Table 2 the backstitched B-scans have a reduced duty-cycle ranging from 27.6% for 0.64 ms to 36.8% for 5.00 ms. Conventional phase-resolved OCT on the other hand has a duty-cycle of 95%. In comparison the backstitched B-scan method has therefore a lower effective acquisition speed by at least a factor of 2.6 compared to conventional phase-resolved OCT.

Using the backstitched B-scans, the *in vivo* phase-noise was measured in the RPE-layer of a healthy volunteer. The mean \pm the standard deviation of the phase-noise is reported in Table 2 which was calculated from 18 B-scans that were randomly placed in the macular region. The measured phase-noise matched the predicted phase-noise as derived in section 3.3 reasonably well. The conventional phase-resolved OCT method shows increased measured phase-noise compared to the predicted phase-noise due to the reduced spot-overlap in this method. At the time intervals 0.64 ms and 1.25 ms a slight increase in the phase-noise was observed which is attributed to the increased location revisit error for high scan frequencies.

Table 2. Backstitched B-scan parameters for the time intervals used in this study. All backstitched B-scans covered a width of 2.1 mm on the retinal surface. The time interval 0.01 ms used conventional phase-resolved OCT without backstitched B-scans. All numbers that are expressed in #A-scans can be converted to time by division through the swept-source repetition rate: 100,000 A-scans/s. The predicted phase-noise was obtained in section 3.3 in which spot-overlap mismatch was minimal.

Time interval (ms)	0.01	0.64	1.25	2.50	3.75	5.00
# A-scans / complete B-scan	-	64	125	250	375	500
# A-scans / B-scan w/o flyback	-	50	100	200	300	400
# A-scans / B-scan flyback	-	14	25	50	75	100
# A-scans in overlap	-	20	20	30	30	30
# sets of repeated B-scans	-	18	8	4	3	2
# A-scans / backstitched B-scan	2000	1920	2000	2000	2250	2000
# A-scans / reconstructed B-scan	1900	530	625	670	810	735
Doppler B-scan duty cycle (%)	95.0	27.6	31.3	33.5	36.0	36.8
#A-scans large flyback	100	208	340	290	285	230
Measured phase-noise (rad)	0.26 ± 0.01	0.39 ± 0.04	0.43 ± 0.09	0.48 ± 0.06	0.49 ± 0.08	0.55 ± 0.08
Predicted phase-noise (rad)	0.13 ± 0.02	0.30 ± 0.09	0.37 ± 0.12	0.47 ± 0.16	0.55 ± 0.19	0.62 ± 0.22

5. Imaging of vasculature

5.1 Pre-processing

Before en-face images of the vasculature were created the acquired data was pre-processed. First the inter-B-scan phase-difference image was calculated from the two reconstructed B-scans. Figure 6(A) displays the inter-B-scan phase-difference image that was obtained from Fig. 5(B) and 5(C). Next the absolute phase-difference image was calculated to avoid the cancellation of positive and negative flow velocities during succeeding processing steps (Fig. 6(B)). Further, false indications of flow in regions with low SNR were prevented by applying a SNR threshold below which the absolute flow was set to zero (Fig. 6(C)). Finally a median filter and a threshold on absolute phase-difference of 0.3 rad (see Table 2) were used to minimize the remaining phase-noise (Fig. 6(D)). The resulting image shows clear distinct dots in the retina for flow in small vessel cross-sections. In the choroid on the other hand a dense layer of flow is seen.

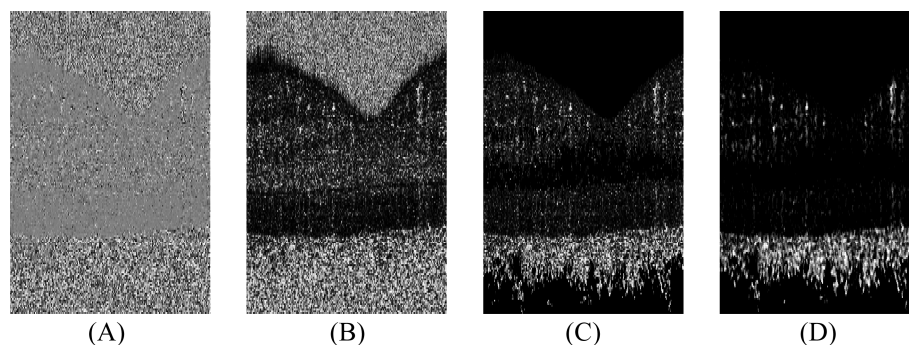


Fig. 6. Pre-processing of inter-B-scan phase-difference images. (A) The inter-B-scan phase-difference image as calculated from Fig. 5(B) and 5(C). (B) The absolute phase-difference is calculated to avoid cancellation of positive and negative flows. (C) A threshold on the SNR is applied to reject noise from low SNR regions. (D) Median filtering and a threshold on the absolute phase-difference are used to minimize remaining phase-noise. Flow in the retinal vessels are visible as white dots, flow in the choroid is visible as a dense white band.

5.2 Imaging of flow in the fovea

The vasculature in the fovea of the left eye of a healthy volunteer was imaged over an area of $2.1 \times 2.1 \text{ mm}^2$ with 300 backstitched B-scans. The measurement time of a single 3D data set was ≤ 6.75 seconds. The retina was segmented using edge-detection of the vitreous-retina and RPE-choroid boundaries in the intensity images. Subsequently the choroid was segmented by considering a $145 \text{ }\mu\text{m}$ thick layer down from the RPE-choroid boundary. En-face images of the retinal and choroidal flow were created by integration over depth of the segmented areas for all B-scans.

In Fig. 7 en-face images of the retinal vasculature in the fovea are displayed at various time intervals. White horizontal lines indicate eye motion artifacts caused by micro-saccades which also caused jumps in the imaged vasculature pattern. Since only small arteries, small veins and capillaries are present in the center of the macula the conventional phase-resolved OFDI method was unable to show any vasculature (Fig. 7(A)). A time interval of 0.64 ms showed several small vessels and even some capillaries that outline the avascular zone (Fig. 7(B)). The density of the observed vasculature further increased for longer time intervals of 1.25 ms up to 5.00 ms (Fig. 7(C)–7(F)). The improvement in the visualized vasculature for time intervals above 2.50 ms is however minimal. These observations are in agreement with the time interval ranges calculated in section 3.4.

Figure 8 shows en-face images of the choroidal vasculature taken with time intervals of 0.01 ms , 0.64 ms and 1.25 ms and were derived from the same data sets as Fig. 7(A)–7(C). The high flow velocities within the choroidal vasculature are partially visible with the lowest time interval (Fig. 8(A)). Any longer time interval results in the visualization of a dense vessel network for which it is hard to identify individual vessels or vascular types. This in agreement with section 3.4 where a time interval of 0.64 ms was calculated to be enough to simultaneously observe all choroidal vascular types. Imaging with time intervals beyond 1.25 ms resulted in almost uniform layers of flow without further imaging advantage and are therefore not displayed.

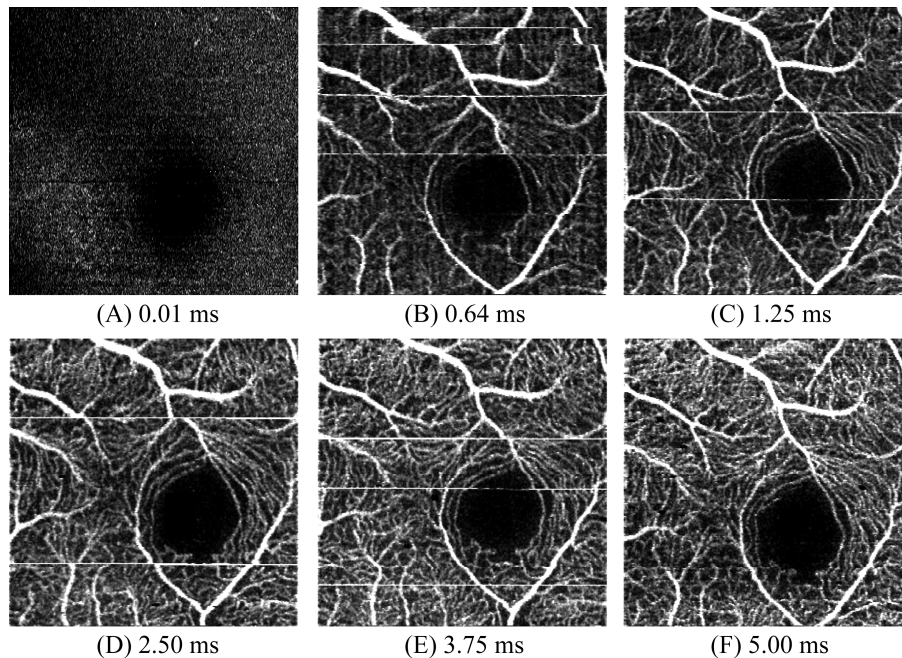


Fig. 7. En-face flow images of the retina in the macular area for a $2.1 \times 2.1 \text{ mm}^2$ area. Increasing time intervals of 0.01 ms (A), 0.64 ms (B), 1.25 ms (C), 2.50 ms (D), 3.75 ms (E), and 5.00 ms (F) were used to improve the visualization of the capillary network, which is optimal for time intervals $\geq 2.50 \text{ ms}$. White horizontal lines indicate eye motion artifacts.

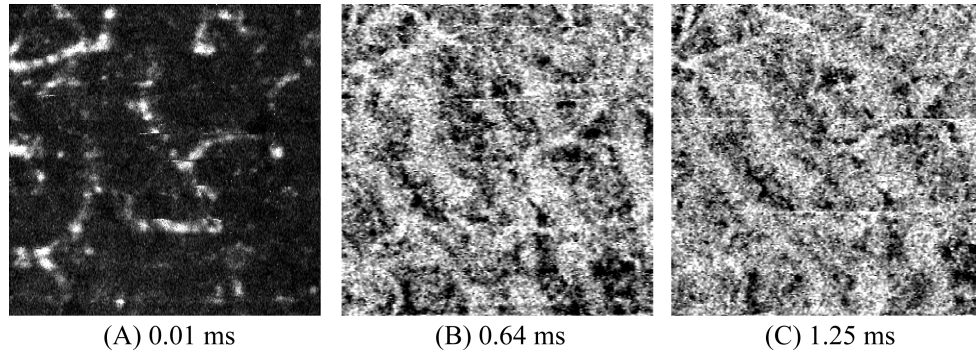


Fig. 8. En-face flow images of the choroid in the macular area for a $2.1 \times 2.1 \text{ mm}^2$ area. Increasing time intervals of 0.01 ms (A), 0.64 ms (B), 1.25 ms (C) were used for a better visualization of the blood flow. The shown images were derived from the same data sets as for Figs. 7(A)–7(C). The fast flow of the choroid is only partly visible with the shortest time interval while longer time intervals reveal a dense vessel network.

5.3 Wide-field flow imaging of the macula and the optic nerve head

In order to evaluate the vasculature outside the fovea, wide-field images were made over an area of $6.0 \times 7.9 \text{ mm}^2$ ($20^\circ \times 26^\circ$) from the left eye of the same healthy volunteer. The wide-field images were created from 12 data sets of $2.1 \times 2.1 \text{ mm}^2$ areas which were all measured two times and combined manually. Since eye motion artifacts are unlikely to occur at the same location for different data sets, the two data sets of each area were combined to reduce the amount of artifacts in the final images. A few eye motion artifacts are however still present.

Wide-field en-face images of the retinal vasculature are shown up to a time interval of 2.50 ms in Figs. 9(A)–9(D). The shortest time interval of 0.01 ms shows the central retinal arteries and veins which possess the highest flow velocities and enclose the macula (Fig. 9(A)). The strength of the flow signal is however varying along the vessels due to the cardiac cycle and changes in vessel orientation with respect to the incoming OCT beam. The time interval of 0.64 ms shows no signal loss along the central vessels and further visualizes the vascular network including smaller arteries and veins that branch off (Fig. 9(B)). Although a few capillaries can be seen around the avascular zone they are absent in the periphery. The visualization of the capillaries is significantly improved for the time interval of 1.25 ms for which also in the periphery capillaries are observed (Fig. 9(C)). However, at some locations the capillary beds are not fully visible as for instance temporal to the avascular zone. Finally, the capillary beds are completely visualized for a time interval of 2.50 ms (Fig. 9(D)). The retinal shadowgram [43] is given for comparison in Fig. 9(E). This image is created by integration of the intensity information in between the retinal nerve fiber layer and the choroid and shows the shadows of the retinal vasculature. The shadowgram is however not able to show capillary structures, which demonstrates the advantage of phase-resolved imaging. High-resolution formats of the wide-field retinal images can be downloaded via the link given in the caption of Fig. 9.

Wide-field en-face images of the choroidal vasculature are shown in Fig. 10 for time intervals up to 1.25 ms. Similar to the retina, discontinuous vessel structures were observed in the choroid for the time interval of 0.01 ms (Fig. 10(A)). Further several localized spots of flow can be seen that are likely due to axially oriented vessels. A dense vascular network was observed when using a time interval of 0.64 ms (Fig. 10(B)). In the center of the macula several thick vessels could be seen while in the periphery thinner vessels were observed. Increasing the time interval to 1.25 ms resulted in an even denser vessels network for which it became hard to identify individual vessels (Fig. 10(C)). As a comparison the integrated intensity en-face image is shown in Fig. 10(D). It is hard to identify individual vessels in this image which is due to insufficient intensity contrast between vessels and surrounding tissues.

Similar to the retina, phase-resolved imaging provides a better view on the choroidal vasculature. High-resolution formats of the wide-field choroidal images can be downloaded via the link in the caption of Fig. 10.

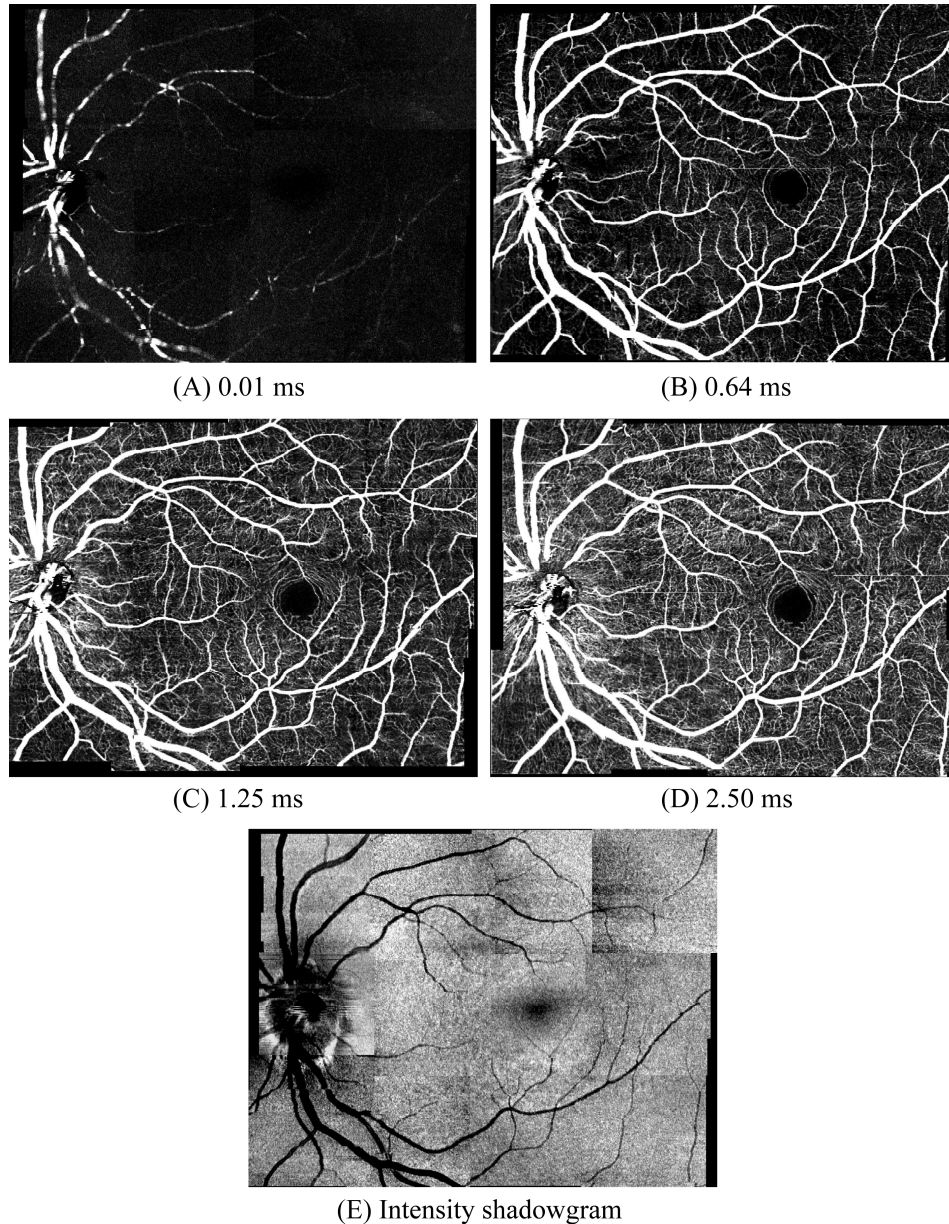


Fig. 9. Wide-field en-face images of blood flow in the retina for a $6.0 \times 7.9 \text{ mm}^2$ ($20^\circ \times 26.3^\circ$) area. Increasing time intervals of 0.01 ms (A), 0.64 ms (B), 1.25 ms (C) and 2.50 ms (D) were used to improve the visualization of the vasculature. For comparison the retinal intensity shadowgram is shown in (E). It can be seen that the shortest time interval shows only the central retinal arteries and veins. The flow signal is however discontinuous along the vessels due to the cardiac cycle and vessel orientation changes. Increasing the time interval gradually shows more of the vasculature including small arteries and veins, arterioles and venules, and capillaries. Although the shadowgram gives a clear view on the central arteries and veins, smaller vasculature cannot be resolved. High-resolution versions of the images can be downloaded here in PDF. ([Media 1](#))

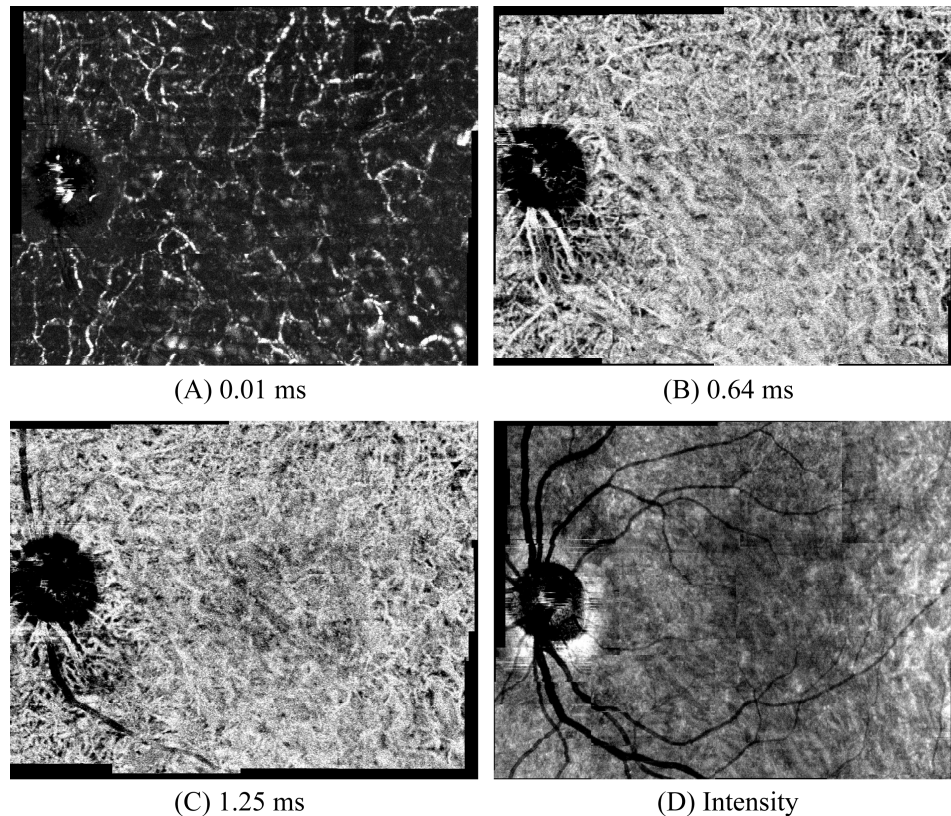


Fig. 10. Wide-field en-face images of blood flow in the choroid for a $6.0 \times 7.9 \text{ mm}^2$ ($20^\circ \times 26.3^\circ$) area. Increasing time intervals of 0.01 ms (A), 0.64 ms (B), and 1.25 ms (C) were used to improve the visualization of the vasculature. For comparison the choroidal intensity en-face image is shown in (D). The shortest time interval shows individual vessels within the choroid, but the flow signal is often discontinuous due to the cardiac cycle and vessel orientation changes. Further several localized spot of flow are seen that are likely due to vertically oriented vessels. Increasing the time interval shows a very dense vascular network. Although individual vessels can be seen it is not possible to distinctly observe the different vascular types. In the integrated intensity en-face image it is hard to identify individual vessels due to insufficient intensity contrast between vessels and surrounding tissues. High-resolution versions of the images can be downloaded here in PDF. ([Media 2](#))

6. Discussion and outlook

6.1 System limitations

A current problem in our implementation of inter-B-scan phase-resolved OCT is eye motion artifacts. Although small slow movements as drift can be tolerated due to the relative large spot-size on the retina, fast large movements from micro-saccades cause significant decorrelation of the compared B-scans. This creates white horizontal artifact lines that for instance can be seen in Fig. 7. Further, the accompanying jumps in the data prohibit a complete view on the vasculature and for now require additional measurements as a patch. Already for the healthy volunteer that was imaged these artifacts occurred frequently with at least 2 failed B-scans or jumps per data set. Patients often have a reduced ability to fixate and it is therefore expected that the amount of artifacts will increase in these cases. A robust solution might be found in the integration of eye tracking hardware in the current setup. Optimal suppression of phase decorrelation requires the spot location to be stabilized within a few microns. Recently, Yang *et al.* showed the stabilization of a stimulus on the retina with an accuracy of 0.15 arcminutes ($\sim 0.75 \mu\text{m}$) using real-time eye motion evaluation and correction

by analyzing the distortion of adaptive optics scanning laser ophthalmoscope images [44]. This technology may achieve the required location stabilization for optimal (SNR-limited) inter-B-scan phase-resolved OCT imaging.

The retinal capillaries have a lumen diameter that ranges between 3.5 μm and 6 μm [34]. In the presented images in this paper the retinal capillaries are however often shown with vessel diameters up to 30 μm . This is a direct consequence of the spot diameter of 25.2 μm and the fact that blood flow is detected as long as (a part of) a capillary falls within the spot. Caution has therefore to be taken when vessel diameters are evaluated. Additionally the large spot-size is inadequate to observe the small openings in the choriocapillaris which can be as small as 5 μm in size [45]. An improved lateral resolution is therefore recommended for future investigations.

The shortest inter-B-scan time interval achieved by our system is limited by the scan speed of the galvanometer scanners to 0.64 ms. This time interval is not able to show the larger choroidal vessels individually for which a time interval of ≤ 0.24 ms (see Table 1) is optimal. A solution to this problem would be to integrate a resonant scanner in the ophthalmic OCT scanning system as shown by Szkulmowski *et al.* [46] or to use either double or multiple beam approaches as shown respectively by Jaillon *et al.* [47] and Leung *et al.* [48].

6.2 Potential clinical applications

Current established tools for angiography of the retina and choroid are fluorescein angiography (FA) and indocyanine green angiography (ICGA). In both methods a dye is injected intravenously to obtain photos of the circulation with high contrast. Adverse reactions to these dyes do occur [49,50] and a non-invasive dye-free method is therefore desirable. Inter-B-scan phase-resolved OFDI is a non-invasive dye-free method and might be a good candidate to replace FA and ICGA for many diagnostic applications. The high resolution and high sensitivity to flow make this technique especially interesting for the detection of early morphological and hemodynamical changes in the retina and choroid which occurs in diseases as e.g. age-related macular degeneration [51] and diabetic retinopathy [35].

6.3 Towards quantitative flow evaluation

Blood flow consists of two directional flow components: axial flow and lateral flow. In axial flow particles move parallel to the incident OCT beam and cause Doppler phase-shifts in the OCT signal. In lateral flow particles move perpendicular to the incident OCT beam. This can cause decorrelation of the OCT signal phase when new particles enter or old particles leave the focus of the OCT beam. Generally, lateral flow is not considered in the evaluation of phase-resolved OCT. However, Koch *et al.* described that lateral movement (flow) over 20% of the spot diameter already causes noticeable deviation from the model described by Eq. (1) [52]. Although this hardly affects the determination of rough time intervals for flow visualization as was done in section 3.4, it will be a problem for accurate flow quantification. Additionally phase-wrapping due to fast axial flow further complicates quantitative analysis.

We therefore propose to use a new intuitive analysis to assess the amount of blood flow based on histogram analysis of volumetric phase-difference data. In phase-resolved OCT the temporal probability distribution of the phase-difference of an individual pixel can be described by a Gaussian distribution. Axial flow will cause a phase-shift and displaces its mean from zero (no flow) to $\Delta\phi$ [19]. Lateral flow will cause an increase of the standard deviation of the Gaussian [53]. The phase-difference of a pixel with flow has therefore a higher probability to be non-zero in contrast to a pixel without flow. For a group of pixels with different spatial locations within a tissue volume the standard deviation of the phase-differences will then be bigger in the case of flow compared to the case without flow. We therefore hypothesize that the standard deviation of a group of pixels is related to the amount of blood flow within the tissue volume.

In order to test our hypothesis, inter-B-scan phase-resolved OFDI with a time interval of 0.64 ms was performed over an area of 2.1 x 2.1 mm² in the macula of a healthy volunteer. Bulk flow velocities were assessed over depth by subdividing the measured volume into

single pixel layer volumes with the RPE-choroid boundary as a reference. Subsequently a histogram of the phase-difference values was taken of each layer, for which an example is shown in the inset of Fig. 11. Interference from non-tissue content was avoided by excluding pixels with a SNR below 5 dB. It can be seen that the histogram follows a Gaussian distribution on top of an uniform distribution. The uniform distribution is attributed to noise. The tails of the Gaussian distribution that extend beyond $\pm \pi$ will wrap back. Therefore, a wrapped Gaussian distribution function including an offset was fitted to the histogram (shown in red) to extract the standard deviation, which we call $\sigma_{\Delta\phi \text{ group}}$ hereafter. For this analysis three different data sets were acquired at the same location. The mean \pm the standard deviation of $\sigma_{\Delta\phi \text{ group}}$ is reported at every depth.

In the main Fig. 11 $\sigma_{\Delta\phi \text{ group}}$ is plotted as a function of depth relative to the RPE-choroid boundary. The depth ranges that are covered by the retina, the RPE, the choroid, and the sclera are marked respectively by lines in red, orange, green and black. The RPE shows the lowest values for $\sigma_{\Delta\phi \text{ group}}$ which is in agreement with the absence of vasculature in this tissue layer. The other retinal tissues show a slight increase in $\sigma_{\Delta\phi \text{ group}}$ due to the modest flow in the small arteries, veins and capillaries. The choroid on the other hand shows a significant higher $\sigma_{\Delta\phi \text{ group}}$ compared to the retina which is caused by the dense vasculature and the high flow velocities within this layer. The choroid further shows a linear increase of $\sigma_{\Delta\phi \text{ group}}$ with depth which indicates the gradual transition from small vessels in the choriocapillaris to large vessels in the lower choroid. Below the choroid $\sigma_{\Delta\phi \text{ group}}$ remains the same in the sclera, which is attributed to the posterior ciliary arteries and veins and possibly Doppler decorrelation shadows from the choroid.

In summary, $\sigma_{\Delta\phi \text{ group}}$ indeed seems to relate to the amount of blood flow within a tissue volume. The proposed quantitative flow analysis might therefore be interesting for studying hemodynamic changes in clinical cases. Especially the distinction between the absence of flow in the RPE and the strong flow in the choroid makes this method promising to study e.g. choroidal flow changes in age-related macular degeneration [51]. However, future research will have to confirm the usability of $\sigma_{\Delta\phi \text{ group}}$ by further theoretical modeling and experimental validation.

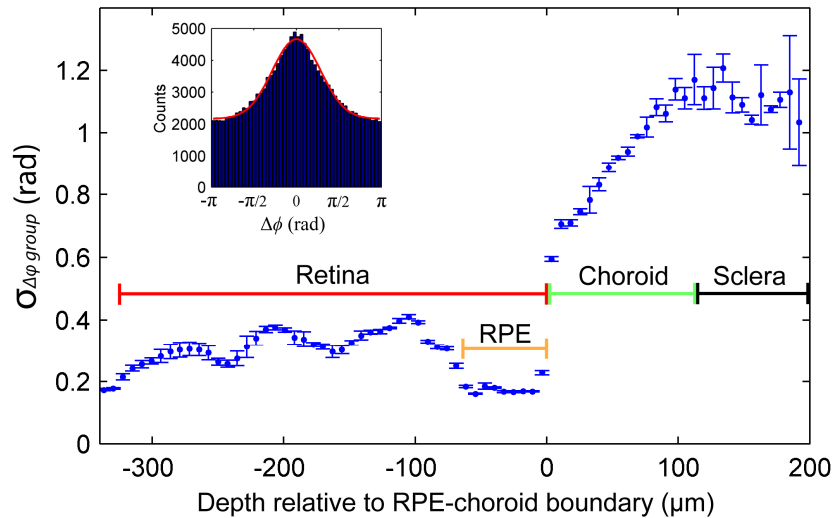


Fig. 11. Schematic description of the proposed flow analysis on volumetric phase-difference data. (Inset) Histogram analysis was performed on the phase-difference values of single-pixel layers. Each layer shows a Gaussian distribution for which the standard deviation, $\sigma_{\Delta\phi \text{ group}}$, is a measure of the amount of blood flow. (Main) A graph of $\sigma_{\Delta\phi \text{ group}}$ as a function of depth which shows absence of flow in the RPE (low values) compared to the rest of the retina (moderate increase) and the choroid (significant increase).

7. Conclusions

In conclusion, we have demonstrated optimized inter-B-scan phase-resolved OFDI for angiography of the retina and the choroid.

A detailed phase-noise analysis was performed on the OFDI system and eye motion was identified as the dominant source of phase-noise and image artifacts. It is expected that real-time eye tracking techniques can significantly reduce the impact of eye motion and will enable vasculature imaging in patients with weak fixation capabilities.

Optimal inter-B-scan time intervals were determined to image the different vascular types in the retina and choroid. The retinal vasculature was imaged down to the capillary level for time intervals ≥ 2.5 ms. In the choroid a very dense vascular network was observed for time intervals ≥ 0.64 ms. Inter-B-scan phase-resolved OFDI was found to perform superiorly to regular phase-resolved OFDI (successive A-scan comparison) and intensity imaging. Inter-B-scan phase-resolved OFDI may therefore be a good candidate to replace dye-based photography in many applications and to study ocular pathologies with early hemodynamic changes.

In addition, a new analysis was proposed to assess the amount of blood flow within a tissue volume with histogram analysis of phase-difference data. This analysis is able to distinguish different flow regimes within the retina and the choroid. Especially for the detection of choroidal flow changes in age-related macular degeneration this method is expected to be valuable.

Acknowledgments

This research was supported by grants from Stichting Wetenschappelijk Onderzoek Oogziekenhuis Prof. Dr. H.J. Flieringa (SWOO), Combined Ophthalmic Research Rotterdam (CORR), and the Dutch MS Research Foundation.